JGR Atmospheres

RESEARCH ARTICLE
10.1029/2021JD035968

Introducing New Metrics for the Atmospheric Pressure Adjustment to Thermal Structures at the Ocean Surface

Agostino N. Meroni[1], **Fabien Desbiolles**[1,2], **and Claudia Pasquero**[1,3]

[1]Department of Earth and Environmental Sciences, University of Milano-Bicocca, Milan, Italy, [2]Osservatorio Geofisico Sperimentale, Trieste, Italy, [3]Institute of Atmospheric Sciences and Climate, Consiglio Nazionale delle Ricerche (ISAC-CNR), Turin, Italy

Key Points:

- The standard metrics for the pressure adjustment mechanism is adversely affected by advection
- Three new metrics are introduced and tested
- The pressure adjustment is detectable in the direction perpendicular to the background wind

Supporting Information:

Supporting Information may be found in the online version of this article.

Correspondence to:

A. N. Meroni,
agostino.meroni@unimib.it

Citation:

Meroni, A. N., Desbiolles, F., & Pasquero, C. (2022). Introducing new metrics for the atmospheric pressure adjustment to thermal structures at the ocean surface. *Journal of Geophysical Research: Atmospheres*, *127*, e2021JD035968. https://doi.org/10.1029/2021JD035968

Received 1 OCT 2021
Accepted 5 AUG 2022

Author Contributions:

Conceptualization: Agostino N. Meroni, Claudia Pasquero
Formal analysis: Agostino N. Meroni
Funding acquisition: Agostino N. Meroni, Claudia Pasquero
Investigation: Agostino N. Meroni, Fabien Desbiolles, Claudia Pasquero
Methodology: Agostino N. Meroni, Fabien Desbiolles, Claudia Pasquero
Supervision: Claudia Pasquero
Writing – original draft: Agostino N. Meroni
Writing – review & editing: Agostino N. Meroni, Fabien Desbiolles, Claudia Pasquero

Abstract Thermal structures at the sea surface are known to affect the overlying atmospheric dynamics over various spatio-temporal scales, from hourly and sub-kilometric to annual and O(1,000 km). The relevant mechanisms at play are generally identified by means of correlation coefficients (in space or time) or by linear regression analysis using appropriate couples of variables. For fine spatial scales, where sea surface temperature (SST) gradients get stronger, the advection might disrupt these correlations and, thus, mask the action of such mechanisms, just because of the chosen metrics. For example, at the oceanic sub-mesoscale, around 1–10 km and hourly time scales, the standard metrics used to identify the pressure adjustment mechanism (that involves the Laplacian of sea surface temperature, SST, and the wind divergence) may suffer from this issue, even for weak wind conditions. By exploiting high-resolution realistic numerical simulations with ad hoc SST forcing fields, we introduce some new metrics to evaluate the action of the pressure adjustment atmospheric response to the surface oceanic thermal structures. It is found that the most skillful metrics is based on the wind divergence and the SST second spatial derivative evaluated in the across direction of a locally defined background wind field.

Plain Language Summary The ocean surface is characterized by a range of warm and cold structures that are known to influence the overlying atmospheric flow through different mechanisms. One of these mechanisms involves the variation of sea level pressure that can drive secondary wind circulations according to how the sea surface temperature is distributed in space. To assess whether this mechanism is in action, the co-location of sea temperature maxima (or minima) with zones of wind convergence (divergence) is generally considered. However, the presence of the wind itself has been shown to displace and delay the wind response so that there are cases where the pressure field responds to the sea temperature forcing but this is not detected by the standard metrics. Since pressure variability is generated in all directions, we propose to measure this kind of wind response in the direction perpendicular to the background wind in order to avoid the masking effect of the background wind.

1. Introduction

Sea surface temperature (SST) structures are known to affect the marine atmospheric boundary layer (MABL) dynamics via two main mechanisms: Downward Momentum Mixing (DMM) (Hayes et al., 1989; Wallace et al., 1989) and Pressure Adjustment (PA) (Lindzen & Nigam, 1987). In the DMM physics, spatial variations of SST modulate the atmospheric stability and the vertical mixing of horizontal momentum, resulting in an acceleration (deceleration) of the surface wind over relatively warm (cold) SST patches. In the PA physics, instead, the thermal expansion (contraction) of air over warm (cold) SST patches is responsible for a spatial modulation of the sea level pressure field that, through secondary pressure gradients, drives surface wind convergence (divergence) over warm (cold) SST structures.

The atmospheric response mediated by these two mechanisms has been observed over different time scales and different regions of the world. Notable examples of observations and theoretical modeling of the MABL atmospheric response over annual and multi-annual scales include Minobe et al. (2008) and Takatama et al. (2015), both of which focus on a PA interpretation of the atmospheric response over the Gulf Stream. In the same region, and over other western boundary currents, other research has applied a DMM physical interpretation at multi-annual (Chelton et al., 2004), seasonal and monthly time scales (Small et al., 2008, and references therein). On the one hand, on scales of the order of few days or even shorter, the works by Chelton et al. (2001), Frenger

et al. (2013) and Gaube et al. (2019) have shown that DMM controls the fast atmospheric response over the Tropical Instability Waves of the eastern Pacific cold tongue, over Southern ocean mesoscale eddies and over a sub-mesoscale filament of the Gulf Stream, respectively. Meroni et al. (2020) and Desbiolles et al. (2021), by looking at 25 years of satellite and reanalysis data, have highlighted the prominent role of DMM on daily scales in affecting both the surface wind response and the subsequent cloud and precipitation signature over SST fronts in the Mediterranean Sea. On the other hand, the observational work of Li and Carbone (2012) argues that PA explains convective rainfall excitation over the western Pacific tropical warm pool on daily scales, and the work by Ma et al. (2020) successfully describes the fast atmospheric response to the cold wakes generated by tropical cyclones in terms of secondary circulations controlled by PA (Pasquero et al., 2021). Thus, there is evidence that both mechanisms contribute to the atmospheric response over a large range of spatio-temporal scales.

Most of the idealized model studies, such as Kilpatrick et al. (2014), Skyllingstad et al. (2007), Spall (2007), and Wenegrat and Arthur (2018), show that DMM is more important than PA over small frontal structures and short time scales. However, several authors suggest otherwise. For example, Skyllingstad et al. (2019) demonstrate that PA is the dominating mechanism in the excitation of convective rainfall on daily scales in the tropical ocean, as observed by Li and Carbone (2012). Lambaerts et al. (2013) show that PA is important over hourly time scales, especially in low background wind conditions. Also Foussard et al. (2019) argue that the PA-mediated fast atmospheric response has been overlooked in the past because the disruptive effect of the advection on the standard metrics has not been properly considered, as described below.

To measure the action of PA, it is common practice to calculate the correlation coefficient or the slope of the linear fit of the binned scatter plots of SST Laplacian and surface wind (or wind stress) divergence (Lambaerts et al., 2013; Meroni et al., 2020; Takatama & Schneider, 2017). Foussard et al. (2019) highlight the shortcomings of considering these two variables, because advection might shift the atmospheric field with the consequent loss of co-location between the SST forcing and the corresponding MABL response might be lost. To overcome this issue, they propose to use the correlation between air temperature Laplacian, rather than SST Laplacian, and wind divergence, showing that PA is as important as (or even more than) DMM in some environmental conditions. However, air temperature is not easy to observe with satellites and, thus, this approach cannot be followed when analyzing remote sensing data.

It is the objective of this study to define and test three new PA metrics that are robust even in the presence of background wind. In particular, these metrics are based on wind field and SST only, which can be retrieved from satellite measurements and for which there are long-term climate data records (Merchant et al., 2019; Verhoef et al., 2017, e.g.). This work is accomplished using a set of high-resolution realistic numerical simulations that have different SST forcing fields. Other than the reference high-resolution experiment, there are two runs with enhanced and reduced SST gradients, and a set of runs with different levels of smoothing of the SST field.

Section 2 describes the numerical model and the performed experiments. Section 3 formally introduces the methods and the new metrics. Section 4 describes the results in terms of skills of the metrics, with a focus on the dependence on the strength of the SST gradients and the spatial scales involved. Section 5 discusses and interprets the results and shows examples of application of the new metrics on annual and seasonal statistics derived from reanalysis and satellite data. Conclusions are drawn in Section 6.

2. Numerical Model and Experiments

A set of high-resolution realistic simulations with artificially modified SST forcing fields (all constant in time) performed with the Weather Research and Forecasting (WRF) model V3.6.1 (Skamarock et al., 2008) are exploited. Its Advanced Research core that solves the fully compressible non-hydrostatic Euler equations is used. The model exploits an Arakawa-C grid in the horizontal and mass-based terrain following vertical coordinates. The grid step of the domain of interest is 1.4 km and there are 84 vertical levels. The full setup includes three domains covering the entire Europe at 12 km grid spacing, the Mediterranean region at 4 km, and the Ligurian Sea at 1.4 km. The outer boundary conditions are forced with the ECMWF-IFS (European Center for Medium-Range Weather Forecasts-Integrated Forecast System) model outputs. The following numerical schemes are used in the simulations: for radiation, the Rapide Radiative Transfer Model (RRTM) for longwaves and the Goddart scheme for shortwaves; for microphysics, the WRF Single-Moment 6-Class scheme; for land surface, the five-layer thermal diffusion scheme; for planetary boundary layer, the Mellor-Yamada Nakanishi Niino level 2.5

Table 1
Summary of the Sea Surface Temperature Forcing Fields of the Various Simulations

Name	SST forcing field
CNTRL	$SST_0(x,y) = \overline{SST} + SST'(x,y)$
UNIF	$\overline{SST}$
ANML_HALF	$\overline{SST} + 0.5 \cdot SST'(x,y)$
ANML_DOUBLE	$\overline{SST} + 2 \cdot SST'(x,y)$
SM1	$G_1 * SST_0(x,y)$
SM2	$G_2 * SST_0(x,y)$
SM4	$G_4 * SST_0(x,y)$
SM8	$G_8 * SST_0(x,y)$
SM16	$G_{16} * SST_0(x,y)$

Note. Symbols are defined in the main text. SST = sea surface temperature.

scheme, together with the revised MM5 similarity for surface layer. All reference papers to these numerical schemes are available online at https://www2.mmm.ucar.edu/wrf/users/physics/phys_references.html. All simulations are initialized at 0000UTC on the 6th of October 2014 and last for four days. A relatively short experimental time frame keeps computational cost low and enables more experiments to be run. In the present work, only the first output of the simulations, taken at 0100UTC on the 6th of October 2014, is considered in the analysis, for reasons discussed in the next section.

The reference simulation is named CNTRL and is forced with a high-resolution SST field, denoted with $SST_0(x, y)$, obtained from a realistic eddy-resolving ocean simulation integrated with ROMS (Regional Ocean Modeling System) in its CROCO (Coastal and Regional Ocean COmmunity model) version (Debreu et al., 2012; Penven et al., 2006), as described in Meroni, Renault, et al. (2018). The $SST_0(x, y)$ field contains small-scale features generated by the ocean dynamics on the numerical grid at 1.4 km. The UNIF experiment is run with a spatially uniform SST field, equal to the spatial mean of the CNTRL SST, indicated as $\overline{SST}$, which is a single number. By taking the difference between the CNTRL and the UNIF SST fields, one obtains the SST anomaly, $SST'(x, y) = SST_0(x, y) - \overline{SST}$, which can be increased or reduced to modify the SST gradients. By multiplying the anomaly by a coefficient α and summing back the UNIF SST value, in fact, one gets an SST field with enhanced or reduced SST gradients but with the same mean value as the CNTRL run. The SST fields of the ANML_HALF and ANML_DOUBLE simulations are obtained in this way (with $\alpha = 0.5$ and $\alpha = 2$ respectively) to get halved and doubled SST gradients. Note that the gradients are modified just by changing the SST magnitude, and not its spatial scales. The other set of simulations considered, instead, includes simulations with an increasing degree of smoothing of the SST field starting from the CNTRL case, which is not smoothed at all. A Gaussian filter, valid over sea points only, is used to smooth the SST field with a standard bi-dimensional convolution operation, indicated with $*$. Note that this filter is set to zero after three spatial standard deviations. It is named G_β and, correspondingly, the experiments are named SMβ, with $\beta \in [1, 2, 4, 8, 16]$ indicating the standard deviation of the Gaussian filter in km. For small standard deviations, the actual shape of the filter is triangular, as a small number of points are considered. As mentioned above, the SST forcing fields does not evolve in time in any of the simulations. The names of the simulations considered are summarized in Table 1 and for further details the reader is referred to Meroni, Parodi, & Pasquero (2018).

3. Methods

The effects of the spatial SST structures on the atmospheric dynamics can be directly evaluated by taking the instantaneous difference of the relevant fields from the simulation of interest with respect to the same field from the UNIF simulation. We denote this operation with Δ, so that the ΔSST of the CNTRL run is

$$\Delta\mathrm{SST}_{\mathrm{CNTRL}}(x, y) = \mathrm{SST}_{\mathrm{CNTRL}}(x, y) - \mathrm{SST}_{\mathrm{UNIF}}(x, y). \quad (1)$$

By definition, $\Delta\mathrm{SST}_{\mathrm{CNTRL}}(x, y)$ is the $SST'(x, y)$ field introduced in the previous section. In particular, we consider the first hour of the simulations, so that the trajectories of the UNIF run and of the other runs have not diverged too much because of the chaotic nature of the equations and because of different wave propagation features (e.g., in the surface pressure field). Note that, despite having the same boundary conditions, the different simulations develop different turbulent small-scale features, that break the correlation when looking at instantaneous differences. To directly evaluate the PA mechanism in terms of pressure response due to the SST spatial structure we compute the Pearson ρ correlation coefficient between ΔSLP (sea level pressure) and ΔSST from various simulations. When considering ΔSST and ΔSLP, the Pearson ρ is computed using all values from the valid sea points. To test its statistical significance, the number of effective degrees of freedom N_{eff} is obtained using the auto-correlation length of the SST, which, for the CNTRL simulation, is $\lambda_{\mathrm{SST}} = 38$ km (Meroni, Parodi, & Pasquero, 2018). In particular, $N_{eff} = |\Omega|/\lambda^2_{\mathrm{SST}} \sim 40$, with $|\Omega|$ denoting the area covered by the valid points over the sea. In the null hypothesis of zero correlation, ρ is normally distributed with zero mean and standard deviation

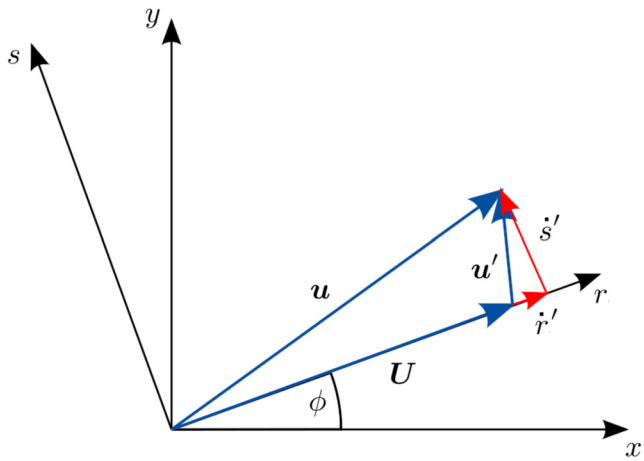

Figure 1. Schematic of the rotated local Cartesian frame of reference $\{r, s\}$ defined according to the large-scale wind vector $\boldsymbol{U}$. The wind anomaly components in the rotated frame of reference $(\dot{r}', \dot{s}')$ are shown with the small red arrows. All symbols are defined in the main text.

equal to $1/\sqrt{N_{eff}}$ (Press et al., 1992). Thus, ρ is statistically significant at the 99% level if it is larger (in absolute value) than $2.57/\sqrt{N_{eff}} \sim 0.4$.

As a benchmark, we compute the standard metrics used in the literature to measure the action of the PA mechanism (Foussard et al., 2019; Meroni, Parodi, & Pasquero, 2018; Takatama & Schneider, 2017): the correlation between wind divergence δ and SST Laplacian Λ, written in spherical coordinates as

$$\delta = \frac{1}{R\cos\theta}\frac{\partial u}{\partial \varphi} + \frac{1}{R\cos\theta}\frac{\partial}{\partial \theta}(v\cos\theta), \tag{2}$$

$$\Lambda = \frac{1}{R^2\cos^2\theta}\frac{\partial^2 \mathrm{SST}}{\partial \varphi^2} + \frac{1}{R^2\cos\theta}\frac{\partial}{\partial \theta}\left(\frac{\partial \mathrm{SST}}{\partial \theta}\cos\theta\right). \tag{3}$$

Longitude φ and latitude θ are defined over a sphere of radius $R = 6{,}371$ km.

In order to introduce the new metrics, a local Cartesian frame of reference based on the background wind field is defined. In particular, the wind components (u, v) can be written as the sum of a large-scale wind (U, V) and an anomaly (u', v'), so that

$$u = U + u'; \quad v = V + v' \tag{4}$$

in the standard local Cartesian frame of reference $\{x, y\}$, with x increasing eastward and y increasing northward. Another instantaneous local Cartesian frame of reference $\{r, s\}$ can be defined according to the large scale wind vector (U, V), whose precise definition is given later, with r being the along-wind direction and s the across-wind direction (positive at 90°counter-clockwise with respect to r), as sketched in Figure 1. With such a definition, a vector (a_x, a_y) in the $\{x, y\}$ frame is readily transformed in the $\{r, s\}$ frame with a standard rotation, namely

$$a_r = a_x\cos\phi + a_y\sin\phi; \quad a_s = -a_x\sin\phi + a_y\cos\phi, \tag{5}$$

with $\cos\phi = U/|\boldsymbol{U}|$ and $\sin\phi = V/|\boldsymbol{U}|$. In particular, the wind field in the new frame of reference is

$$\dot{r} = u\cos\phi + v\sin\phi; \quad \dot{s} = -u\sin\phi + v\cos\phi, \tag{6}$$

And, by definition, can be decomposed as

$$\dot{r} = |\boldsymbol{U}| + \dot{r}'; \quad \dot{s} = \dot{s}'. \tag{7}$$

With the same approach, by projecting the gradient $\nabla\psi$ of a given quantity ψ onto the new directions $\{r, s\}$, one gets the derivatives with respect to r and s as

$$\frac{\partial \psi}{\partial r} = \hat{\boldsymbol{r}}\cdot\nabla\psi; \quad \frac{\partial \psi}{\partial s} = \hat{\boldsymbol{s}}\cdot\nabla\psi, \tag{8}$$

with $\hat{\boldsymbol{r}}$ and $\hat{\boldsymbol{s}}$ being the unit vectors of the new coordinates. In particular, using $\{\varphi, \theta\}$, the local rotation with respect to the large-scale wind is the same as for the local standard Cartesian frame of reference $\{x, y\}$ as in Equation 5 and, thus,

$$\frac{\partial \psi}{\partial r} = \frac{\cos\phi}{R\cos\theta}\frac{\partial \psi}{\partial \varphi} + \frac{\sin\phi}{R}\frac{\partial \psi}{\partial \theta}; \tag{9}$$

$$\frac{\partial \psi}{\partial s} = \frac{-\sin\phi}{R\cos\theta}\frac{\partial \psi}{\partial \varphi} + \frac{\cos\phi}{R}\frac{\partial \psi}{\partial \theta}. \tag{10}$$

In the rotated frame of reference new quantities are defined: the across-wind divergence

$$\delta_s = \frac{\partial \dot{s}'}{\partial s} = \frac{\partial \dot{s}}{\partial s} \tag{11}$$

And the across-wind SST Laplacian

$$\Lambda_s = \frac{\partial^2 \mathrm{SST}}{\partial s^2}. \tag{12}$$

In a similar way, the along-wind divergence

$$\delta_r = \frac{\partial \dot{r}'}{\partial r} \tag{13}$$

And the along-wind SST Laplacian

$$\Lambda_r = \frac{\partial^2 \mathrm{SST}}{\partial r^2} \tag{14}$$

can be introduced. Note that in the along-wind divergence δ_r the large scale wind is removed because, by definition, it is a smooth field and does not respond to the small-scale SST structures, which are the main focus of the present work.

The strength of using this rotated frame of reference to detect the PA mechanism comes from the fact that pressure is a scalar and produces gradients and, possibly, a dynamical response in all directions. In fact, by looking at the across-wind direction, it is possible to remove the effects of the large-scale advection, which are known to mask the PA signal (Foussard et al., 2019; Lambaerts et al., 2013). Schneider (2020) also exploits a local frame of reference based on the background wind to compute the response and the transfer functions (that can be considered the bi-dimensional extensions of the coupling coefficient in the physical and the spectral spaces, respectively) to various SST forcings. This proves to be a relevant frame of reference to characterize the atmospheric response.

Another approach to reduce the effect of advection is to stretch the coordinates $\{x, y\}$ along the direction of the large-scale wind using the following transformation

$$x_\star = \frac{x}{|U|}; \quad y_\star = \frac{y}{|V|}. \tag{15}$$

This means that $\{x_\star, y_\star\}$ are time coordinates and can be used to introduce the stretched wind divergence $\delta_\star$ and the stretched divergence of the SST gradient, which is named stretched SST Laplacian $\Lambda_\star$. In spherical coordinates they are written as

$$\delta_\star = \frac{|U|}{R\cos\theta}\frac{\partial u}{\partial \varphi} + \frac{|V|}{R\cos\theta}\frac{\partial}{\partial \theta}(v\cos\theta), \tag{16}$$

$$\Lambda_\star = \frac{|U|}{R^2\cos^2\theta}\frac{\partial^2 \mathrm{SST}}{\partial \varphi^2} + \frac{|V|}{R^2\cos\theta}\frac{\partial}{\partial \theta}\left(\frac{\partial \mathrm{SST}}{\partial \theta}\cos\theta\right). \tag{17}$$

Alternatively, to focus on the small-scale response, one can remove the large scale wind and compute the divergence of the wind anomaly (u', v'), namely

$$\delta' = \frac{1}{R\cos\theta}\frac{\partial u'}{\partial \varphi} + \frac{1}{R\cos\theta}\frac{\partial}{\partial \theta}\left(v'\cos\theta\right), \tag{18}$$

which is named wind divergence prime. This is equivalent to the sum of the across-wind and the along-wind divergence defined above

$$\delta' = \delta_r + \delta_s, \tag{19}$$

as the horizontal divergence does not depend on the local rotation of the frame of reference. As for the along-wind divergence δ_r introduced above, δ' does not consider the large-scale wind divergence, which is a relatively smooth field and should be independent of the small-scale spatial SST features.

In what follows, the large-scale wind is computed using a bi-dimensional Gaussian filter on the valid points over the sea with a standard deviation of 10 grid steps (roughly 14 km), unless stated otherwise. A sensitivity to this value is discussed in the next section. A coastal strip of roughly 20 km is removed from the analysis, to avoid

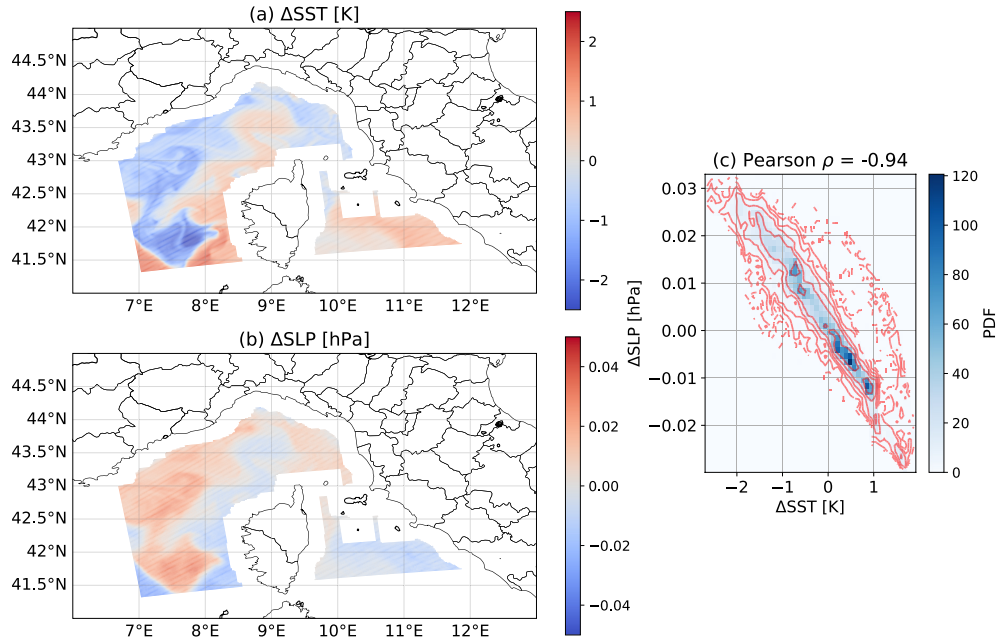

Figure 2. Instantaneous maps of (a) ΔSST and (b) ΔSLP from the CNTRL simulation at 0100UTC on the 6th of October 2014. (c) Bi-dimensional distribution of the same variables shown with colors as a normalized probability density function (PDF). The red lines indicate the contours of the logarithm of the same PDF.

including some features that develop in the first few hours of the simulation with numerical waves propagating from the coastlines over the sea. As the next section shows, this does not prevent to detect the local atmospheric response to small-scale SST features.

Two kinds of correlation coefficients are considered: the Pearson ρ and the Spearman r, which is the Pearson correlation coefficient calculated using the ranking of the values, instead of the values themselves (Press et al., 1992). While the Pearson ρ coefficient measures the linearity of the relationship between the two variables under study, the Spearman r measures how much their relationship is monotonic. The statistical significance of the Spearman r coefficient is assessed with a Student-t test (Press et al., 1992). The correlation coefficients are computed either directly on the pointwise values of the relevant fields or on averaged values in classes of percentiles (introduced below). By computing the correlation coefficient using percentile classes one can robustly assess whether the PA mechanism is acting or not, while with the coupling coefficient one can measure the strength of the atmospheric response.

In the literature, binned scatter plots have been used to measure the strength of the air-sea coupling, by computing their slope to get the so-called coupling coefficients (Chelton & Xie, 2010; Renault et al., 2019; Small et al., 2008, e.g.,). As the least-square estimate of the linear trend is not robust with respect to the presence of outliers, the extreme values in the binned scatter plot can control the value of the coupling coefficient, especially when instantaneous data are considered. To avoid this, the data are organized into percentile bins, so that the statistics are computed over bins with the same number of points, as in Desbiolles et al. (2021). In particular, we compute the mean value and standard error of the dependent variable (y axis) conditioned to the percentile bins of the control variable (x axis). All figures and coefficients shown in this work are computed using 20 bins containing 5% of the points each. The results were tested not to be sensitive to this choice by considering bins with 2% and 10% of the points (not shown).

4. Results

By looking at the correlation between ΔSST and ΔSLP from the CNTRL simulation we can directly evaluate the pressure response to the presence of small-scale SST features because small SLP anomalies are introduced that are highly correlated to the SST anomalies (Figure 2). In particular, a strong correspondence between the ΔSST and ΔSLP fields is visible in the maps of panels (a) and (b). This is confirmed by the high (in absolute value) and

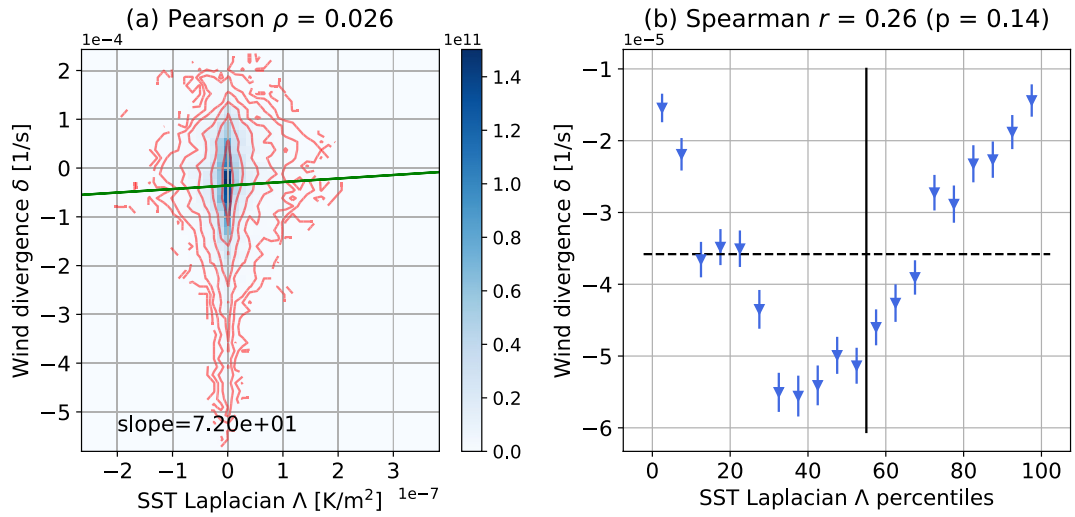

Figure 3. (a) Bi-dimensional distribution and (b) percentile scatter plot of the sea surface temperature (SST) Laplacian and the wind divergence from the CNTRL experiment. In (b) the error bars show the standard error of the bins, the vertical line indicates where the SST Laplacian changes sign and the horizontal dashed line the mean value of the wind divergence.

statistically significant (>99%) Pearson $\rho = -0.94$ obtained between the same two fields. This suggests that PA is acting on hourly scales over fine SST structures at midlatitudes, as in the present experiments.

A correlation visually appears also between SST Laplacian Λ of the CNTRL run and $\Delta\delta_{\mathrm{CNTRL}}$ fields (not shown), indicating that such small-scale pressure anomalies rapidly force surface wind convergent and divergent cells, in agreement with the physics of PA. However, the correlation between SST Laplacian and wind divergence (without taking the difference with respect to the UNIF simulation, namely, without removing the large-scale signal) taken from the same instant of the CNTRL simulation is very low (Figure 3). In particular, from the bi-dimensional distribution (panel (a)) it is clear how wind divergence is unrelated to the SST Laplacian, especially for very low values of SST Laplacian. The two fields have a very low Pearson ρ, which indicates that the wind divergence variance explained by the linear model as a function of the SST Laplacian is very low ($\rho^2 \sim 0.1\%$). This is physically related to the fact that the atmospheric dynamics is controlled by many processes that have nothing to do with the SST field. A monotonic relationship is not apparent between wind divergence and SST Laplacian (Figure 3b). This is confirmed by the low and non-significant (at the 99% level) Spearman $r = 0.26$ coefficient calculated on the percentile scatter plot. It is worth highlighting that the particular shape of the percentile scatter plot of panel (b) observed here is not a general feature (as it depends on the season, the region and, likely, some environmental conditions) and will not be discussed further.

The bi-dimensional distribution and percentile scatter plot of the three new metrics are computed (Figure 4). The advantages of considering the across-wind direction to detect the PA atmospheric response emerge (panels (a) and (b)). In fact, the bi-dimensional distribution of the across-wind divergence and the across-wind SST Laplacian, panel (a), appears to be more symmetric with respect to the origin and shows a slight tilt far from the zero across-wind SST Laplacian (as highlighted by the linear regression line). The Pearson $\rho = 0.038$ is still low and not significant at the 99% percent level. The tilt visible in the bi-dimensional distribution, that corresponds to increasing across-wind divergence for increasing across-wind SST Laplacian, becomes more evident in the percentile scatter plot (panel (b)). This is found to have a high Spearman $r = 0.85$, statistically significant at the 99% level, indicating that the trend is truly positive. It is interesting to highlight that for very negative (positive) across-wind SST Laplacian, across-wind surface wind convergence (divergence) is found, in agreement with the action of the physical mechanism.

The use of stretched coordinates does not alter the low correlation values (Pearson or Spearman) for detecting PA (panels (c) and (d)). Moreover, no divergence is ever observed in the percentile scatter plot values, not even at the highest percentiles. This is due to the presence of a large-scale negative divergence component, which also emerges in the wind divergence field shown in Figure 3, that causes the mean value to be negative. This is confirmed by the distributions of the wind divergence prime field (panels (e) and (f)). In fact, it appears that the

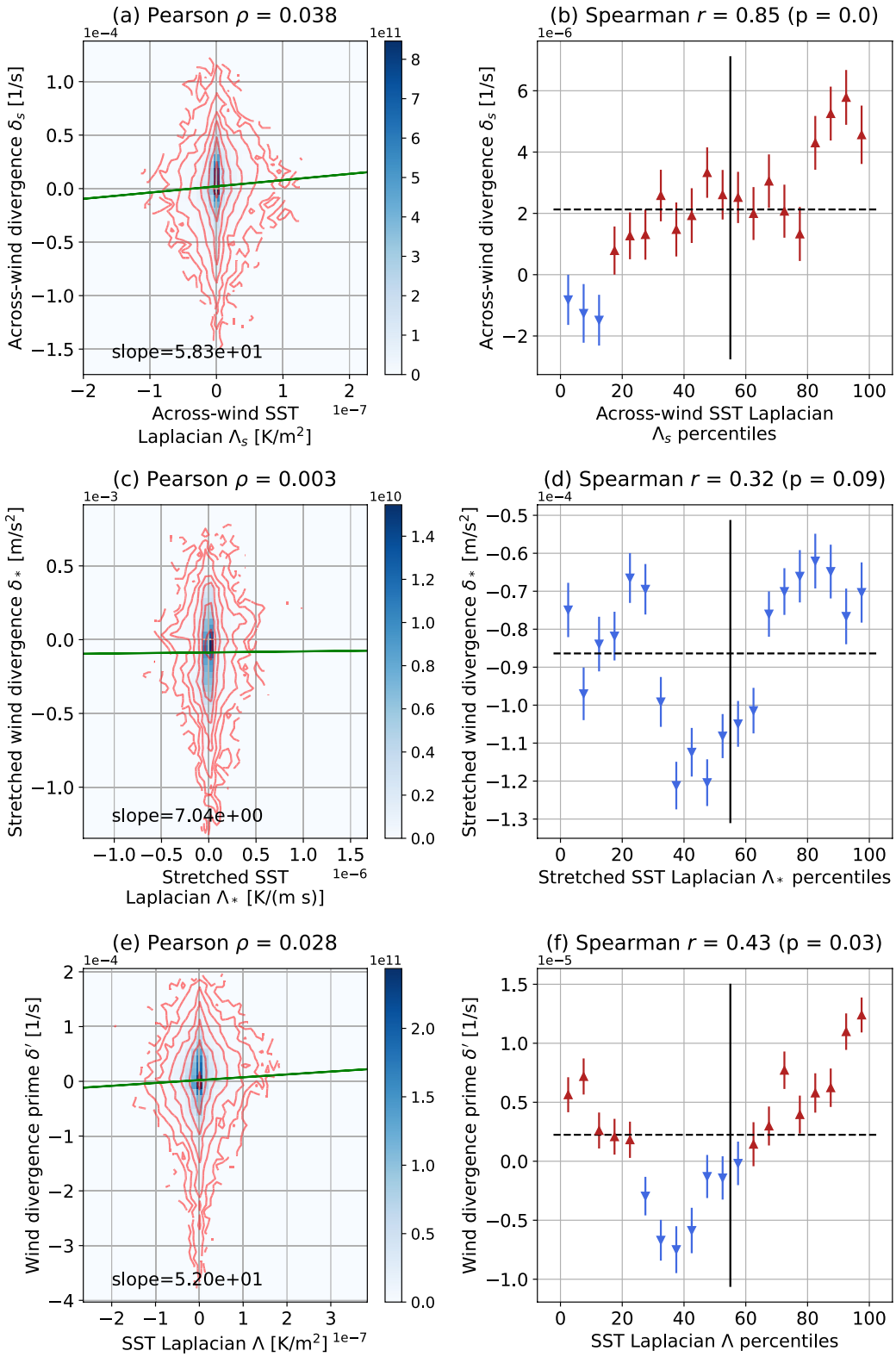

Figure 4. Bi-dimensional (left column) and percentile (right column) distributions of: (a–b) across-wind sea surface temperature (SST) Laplacian Λ_s and across-wind divergence δ_s; (c–d) stretched SST Laplacian $\Lambda_\star$ and stretched wind divergence $\delta_\star$; (e–f) SST Laplacian Λ and wind divergence prime δ'. In (a, c, and e) the blue shades indicate the probability density function (PDF) and the red lines indicate the log of the PDF. The least-square linear fit is also displayed with a green line. In (b, d, and f) the horizontal lines denote the sample average of the variable displayed on the *y* axis and the vertical lines indicate where the variable on the *x* axis changes sign.

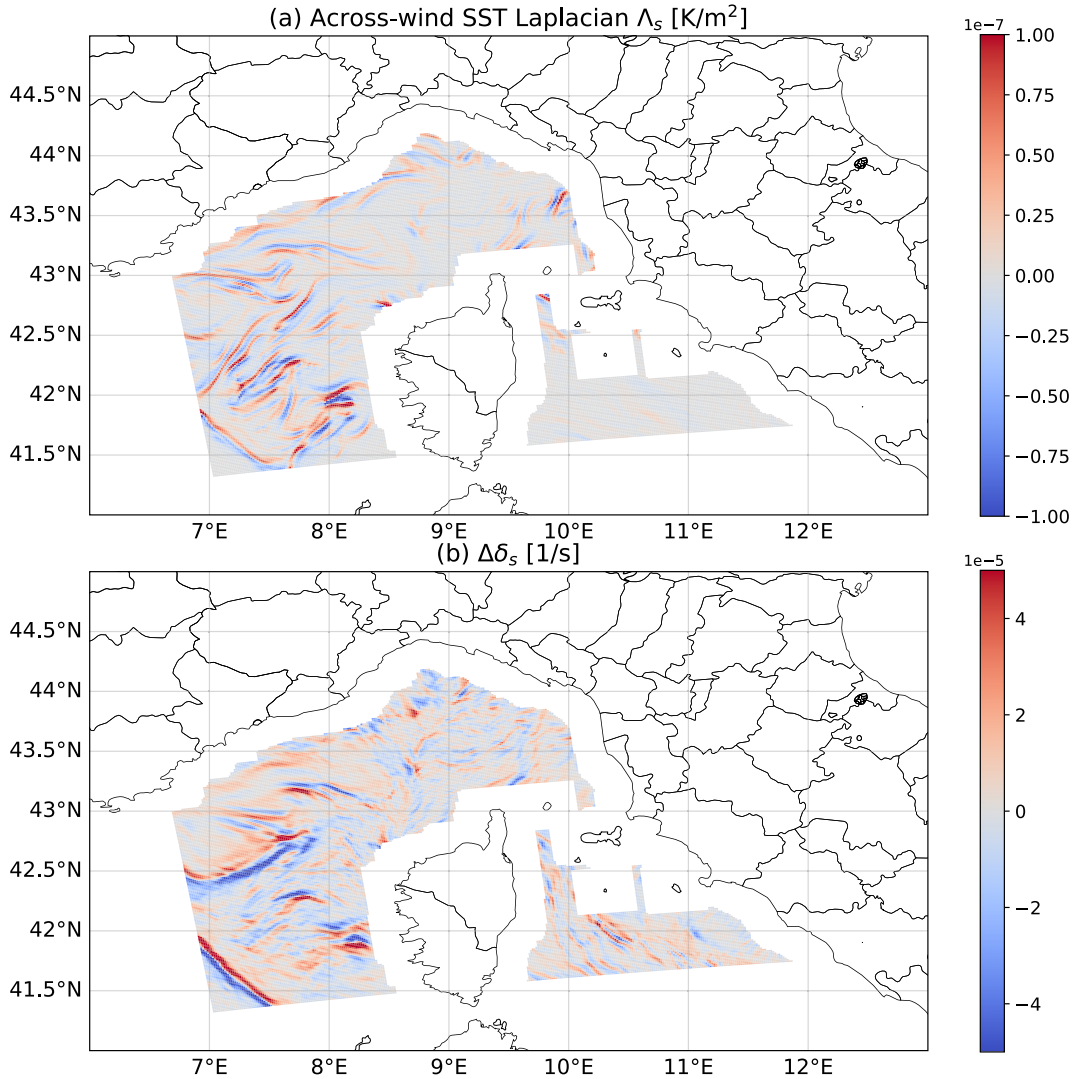

Figure 5. Maps of (a) across-wind sea surface temperature Laplacian Λ_s from the CNTRL case and (b) $\Delta\delta_s$, the difference of the across-wind divergence from the CNTRL case and the UNIF case, with the large-scale wind used to defined the rotated frame of reference $\{r, s\}$ coming from the CNTRL simulation.

mean wind divergence prime ($\sim 0.25 \times 10^{-5}$ s^{-1}) is an order of magnitude closer to zero than the mean wind divergence ($\sim -3.5 \times 10^{-5}$ s^{-1}), indicating that the negative bias of the wind divergence and the stretched wind divergence fields is really due to the large-scale. Also the us of wind divergence prime (i.e., removing the large-scale wind) in the calculation of the correlation coefficients is not enough to highlight the small-scale atmospheric response controlled by PA. In fact, both the Pearson $\rho = 0.028$ and the Spearman $r = 0.43$ are relatively low and not significant at the 99% level.

An adjustment to the small-scale wind divergence field caused by PA is noted by looking at the across-wind SST Laplacian (Figure 5a) and the difference between the across-wind divergence of the CNTRL case and the UNIF case, $\Delta\delta_s$ (Figure 5b).

4.1. Dependence on the Strength of the SST Gradients

The set of experiments that includes ANML_HALF, CNTRL and ANML_DOUBLE are now analyzed. According to the definition of their forcing SST fields, they all have the same spatial mean SST value (equal to the uniform SST used in the UNIF case), with unchanged spatial scales and the SST gradients increasing by a factor

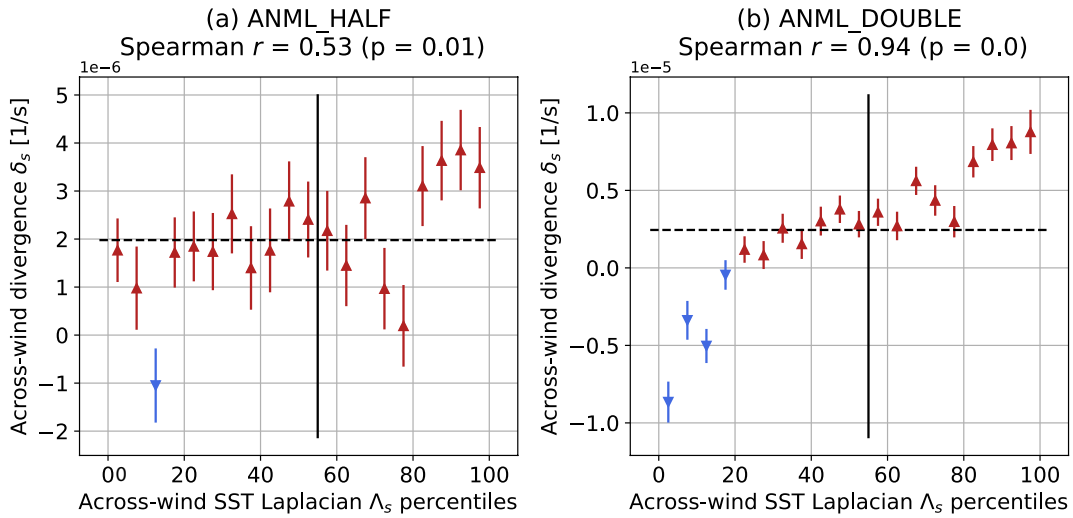

Figure 6. Percentile scatter plots of across-wind sea surface temperature (SST) Laplacian and across-wind divergence from the ANML_HALF (a) and ANML_DOUBLE (b) simulations. The vertical lines indicate the change of sign of the across-wind SST Laplacian and the horizontal dashed lines indicate the mean across-wind divergence.

of 2. By directly computing the correlation between the ΔSLP and ΔSST fields, we can state that PA is responsible for the atmospheric adjustment irrespective of the strength of the SST gradients, even if they are halved with respect to the CNTRL case. This is proven by the very high (in absolute value) and statistically significant Pearson ρ (at the 99% level) calculated in all three cases (Figure S1 in Supporting Information S1).

The percentile scatter plots of the across-wind variables, Λ_s and δ_s, for the ANML_HALF and ANML_DOUBLE runs show that the new metrics based on the across-wind variables is able to detect a significant correlation (in terms of Spearman r) in both cases (Figure 6). In agreement with the previous results from the CNTRL simulation only, and with the physical understanding of the mechanism, the results from this set of simulations indicate that the surface wind divergence response is enhanced as the spatial variability of SST increases. This implies, then, that the skill of the correlation coefficients to detect the action of the PA mechanism increases with stronger SST variability.

From the bi-dimensional distributions and the percentile scatter plots of the standard variables, SST Laplacian Λ and wind divergence δ, and of the across-wind variables, Λ_s and δ_s, respectively, for the ANML_HALF, CNTRL and ANML_DOUBLE simulations, it appears that the correlations between SST Laplacian and wind divergence are low and non-significant, whereas the correlations between across-wind variables are higher and significant (Figures S2 and S3 in Supporting Information S1. Thus, fine-scale strong SST variations (on the same spatial scale over which the wind dynamics is resolved) have an imprint in the surface wind divergence field on short time scales. By reducing the masking effect of the advection, in particular by looking at the across-wind direction, the PA action can be successfully detected, which is not the case if the standard variables (SST Laplacian and wind divergence) are used. Moreover, the fact that the Spearman r increases going from ANML_HALF to ANML_DOUBLE suggests that the presence of stronger SST variability makes this metric more efficient. More on this aspect is developed in the next section.

4.2. Spatial Scale of the Response

The characteristic length scales of the atmospheric response are now considered. In the first place, considering the CNTRL simulation, two things can be tested: (a) the skills of the standard metrics (based on Λ and δ) as a function of the standard deviation σ of a Gaussian filter used to smooth the SST Laplacian and wind divergence fields themselves, and (b) the skills of the across-wind metrics (based on Λ_s and δ_s) as a function of the standard deviation σ used to define the large-scale background wind field.

The Spearman r between the smoothed standard variables shows that for a very local smoothing (small σ), the correlation is relatively low, ~0.4, while a peak in the correlation is reached with σ between 25 and 30 km

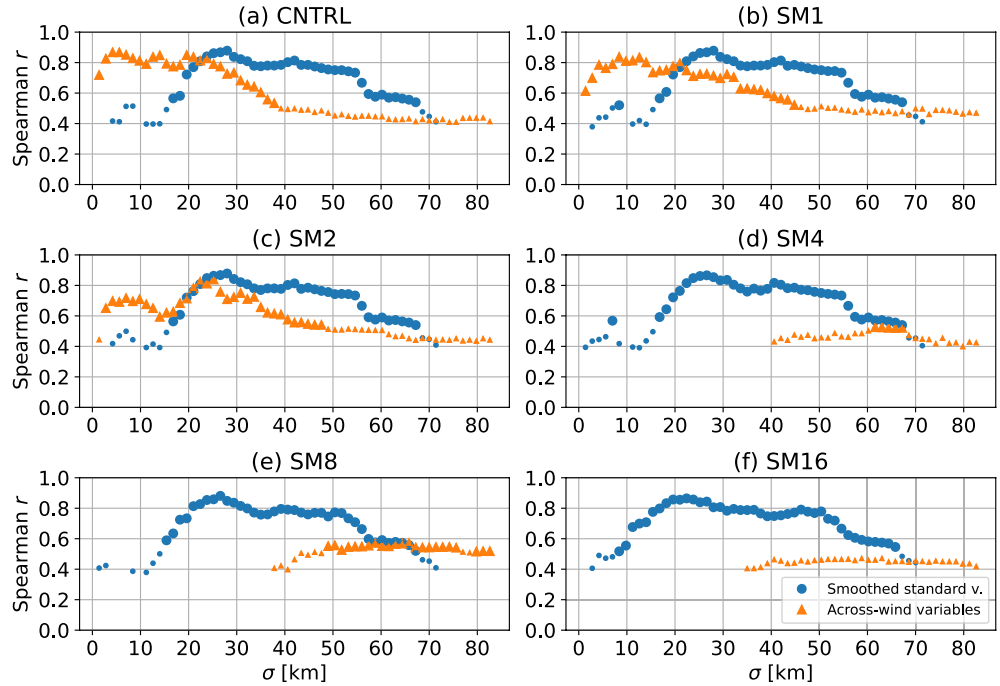

Figure 7. Spearman r coefficients calculated on the percentile scatter plots of the across-wind variables (orange triangles) and of the smoothed standard variables (sea surface temperature (SST) Laplacian and wind divergence, blue circles). The coefficients are shown as a function of the standard deviation σ of the Gaussian filter used either to determine the background wind for the across-wind variables shown with the orange triangles or to spatially smooth the SST Laplacian and the wind divergence shown with the blue circles. The titles of the panel show the names of the simulations considered. Small and large symbols show the coefficients significant at the 95% and 99% level, respectively.

(Figure 7). This is interpreted to be due to a reduced masking effect of the advection when the fields are smoother, linked to a better match between the length scale of the PA atmospheric response and the length scale of the SST forcing, as discussed more in detail in the next section. In the same panel, the across-wind variables show a high and significant correlation up to $\sigma \sim$25 km. With σ between 25 and 40 km the correlation drops and after 40 km it is no longer significant at the 99% level. In the limit of very large σ, the correlation is expected to be similar to the value of the non-filtered standard metric (correlation between the SST Laplacian and the wind divergence), as a uniform background wind is used to compute the across-wind derivatives and no information on the local structure of the flow is retained. This indicates that the metrics based on the across-wind variables is able to detect the PA signal for $\sigma < 25$ km.

By considering the set of simulations with a smoothed SST field, the SMβ set of experiments, the skills of the new metrics when the SST gradients get weaker both because the SST variability decreases and because their spatial scales increase can be tested. Note that the standard deviation of the filter applied to the SST forcing β is completely independent from the standard deviation of the filters applied to the diagnostic fields σ. We verify that the direct atmospheric response in terms of pressure, measured by the Pearson ρ correlation between ΔSLP and ΔSST is strong and significant in all SMβ cases. It is found that the correlation is always lower than -0.91. Thus, despite the SST first and second derivatives get weaker because of the spatial smoothing, the presence of a non-uniform SST introduces a direct atmospheric response in terms of surface pressure. The maps of ΔSLP and ΔSST also confirm the strong correspondence of the two fields (not shown).

Considering smoother SST forcing fields, a consistent behavior of the smoothed standard variables emerges (Figures 7b–7f). In fact, it is always found that a smoothing with a σ of 20–30 km is needed to reduce the advection effect and get the peak in correlation suggesting that the SST forcing at these scales is detected by the atmospheric dynamical response. In terms of across-wind variables, instead, it emerges that when the forcing SST field does not have any small-scale feature (starting from SM4, panel (d), and for higher β), the wind field is not constrained by the SST and the correlation is not significant for $\sigma < 20 - 30$ km. For higher σ, instead, the Spearman r of the across-wind variable tends to the Spearman r of the non-smoothed standard variables (SST Laplacian and wind

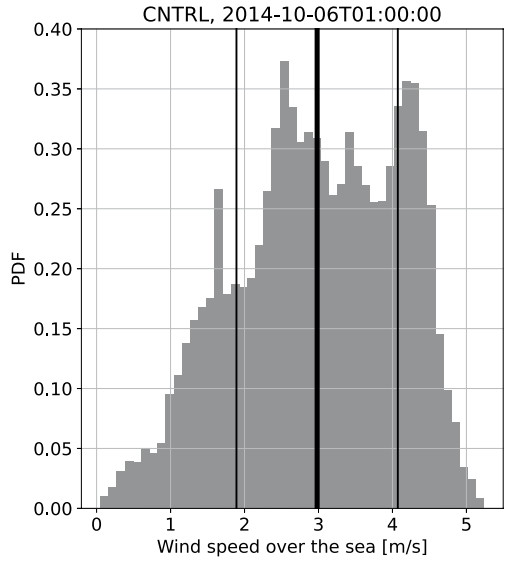

Figure 8. Histogram of the wind speed over the sea from the CNTRL experiment at the instant considered. Vertical lines indicate the mean value (thin line in the middle) and the mean ± one standard deviation.

divergence), as previously discussed. This confirms that the metrics based on the across-wind variables does not detect any small-scale atmospheric response in the case where no small-scale SST forcing is present, which is important to show for the definition of a new metrics.

Note that in the definition of the across-wind divergence δ_s and the primed wind divergence δ' the background wind field is removed. Thus, considering these variables instead of the wind divergence δ is a form of high-pass filter whose cutoff length is determined by σ itself. The larger the σ, the smoother the background wind field, but the wind divergence fields always have a small-scale component. So far, the background wind Gaussian filter has been defined with a standard deviation σ of 10 grid points (equivalent to 14 km), but its values can be used to select the scales of the atmospheric response of interest in the δ_s and δ' fields.

The Spearman r correlation between the percentile scatter plots of the stretched SST Laplacian and the stretched wind divergence has a very weak dependence on the σ used to determine the background wind field for both the CNTRL and all the SMβ runs (not shown). This happens because in the calculation of the stretched variables the large-scale wind is not removed and there is no high-pass filter behavior. For all cases, then, the correlation is never significant at the 99% level. Instead, we do not show the Spearman r correlation between the SST Laplacian and the wind divergence prime δ', because its behavior as a function of σ is similar to the across-wind variables one, with generally lower correlation values.

5. Discussion

The new metrics based on the across-wind variables has been shown to detect the PA signal over hourly time scales in the midlatitudes (Figure 4). This is in agreement with the results of Lambaerts et al. (2013). In their work, they are able to show it by computing the standard metrics (correlation coefficient between the vertical wind velocity, closely related to the horizontal wind divergence, and the SST Laplacian) in some idealized numerical simulation with absent or very weak (1 m s^{-1}) background wind. The fact that here the correlation between the standard variables is low can be explained by the presence of a non-zero background wind (whose histogram is shown in Figure 8). It ranges from 0 to 5 m s^{-1}, with a mean value of 3 m s^{-1} over the sea in the instant considered. In agreement with the arguments presented by Foussard et al. (2019), the presence of a non-zero mean wind breaks the correlation between SST Laplacian and wind divergence.

By considering the simulations with smooth SST fields, then, it has also been shown that when the small scale SST forcing is not present, the new across-wind metric does not detect any atmospheric response, as expected. In fact, as the spatial scale of the SST structures increases (corresponding to high β in the SMβ simulations), the scales of the SST-induced pressure gradients also increase. This means that, at fine scales, the SST structure does not produce any pressure gradient that can alter the wind field, and, thus, the fine-scale wind variability cannot be constrained by the SST. This has been tested by changing the standard deviation of the Gaussian filter used to calculate the background wind speed σ and considering all simulations of the SMβ set (Figure 7).

In the literature, the characteristic time scale of the PA mechanism is written as h^2/K_T, where h is the MABL height and K_T is the thermal eddy turbulent coefficient (Small et al., 2008). Physically, this corresponds to the time required for a non-negligible pressure anomaly to develop, which is controlled by the temperature mixing in the MABL. By looking at the CNTRL simulation, the MABL height is between 300 and 1,400 m, whereas a typical mid-latitude value for K_T is 15 m^2 s^{-1} (Redelsperger et al., 2019). By multiplying the PA time scale by the typical wind speed U_0, one gets the length scale over which PA produces a wind response (Small et al., 2008). In particular, using the mean wind speed of U_0 ~3 m s^{-1} of the instant of the simulation considered (see Figure 8), the PA length scale $L_p \sim U_0 h^2/K_T$ is in the range between 15 and 360 km. The σ of the filter that maximizes the Spearman r between the smoothed SST Laplacian and the smoothed wind divergence, which is around 30 km, falls in this range. In particular, as the extent of the Gaussian filter is actually 3 times its standard deviation, we

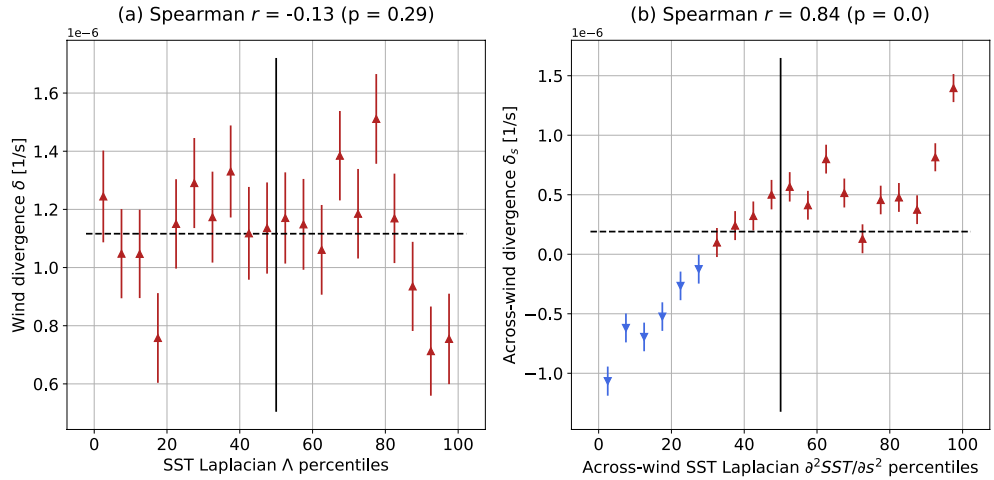

Figure 9. Spring percentile scatter plots (mean and standard error for each bin) calculated over the Mediterranean Sea for (a) sea surface temperature (SST) Laplacian Λ and wind divergence δ, and (b) across-wind Laplacian $\Lambda_s = \partial^2 \mathrm{SST}/\partial s^2$ and across-wind divergence δ_s. The L4 ESA CCI SST analysis product and the L2 METOP-A ASCAT CDR wind field product are used. The horizontal dashed lines denote the mean value of the variable shown on the y axis and the vertical solid lines indicate the percentile where the variable shown on the x axis changes sign.

can consider that the length scale of the structures that maximizes the SST Laplacian and wind divergence correlation is roughly 100 km, which is very close to the mean value of L_p ~120 km. This suggests that the masking effect of the advection on the correlation between SST Laplacian and wind divergence is reduced when some smoothing is performed on the wind field and when the scales of the forcing SST are of the same order as the PA length scale.

In other words, the PA-mediated secondary circulation develops in response to the underlying SST structures on a length scale L_p, which, in the direction of the wind, is large compared to the typical SST structures. Thus, as the response of the air moving with the flow is integrated over the small scale SST variability, it is only sensitive to the smoother and larger scale thermal features. In the across-wind direction, the advection U_0 tends to zero and, thus, the PA length scale L_p tends to zero as well. For this reason, the spatial response mediated by PA can be detected over very small scales by the newly introduced metric, as previously demonstrated.

None of the two other metrics is found to be skillful. In fact, the use of the coordinate stretching does not correspond to any increase in the correlations, because there is no selection of the small scales (accomplished in the other cases with the subtraction of the background wind). Removal of the large-scale wind before computing the wind divergence result in a modest improvement with respect to the full wind divergence field. This is explained by the presence of the effects of the large-scale advection, which keeps the skills of this metrics lower than the across-wind one. This corresponds to the fact that the integral PA-mediated atmospheric response is realized over relatively large L_p scales.

The new metric based on the across-wind variables can also be applied to some high-resolution satellite data. The daily L4 ESA CCI (European Space Agency Climate Change Initiative) SST analysis product v2.1 (Good et al., 2019; Merchant et al., 2019) and the instantaneous L2 coastal METOP-A ASCAT (METeorological OPerational satellite-A Advanced SCATterometer) wind field CDR (Climate Data Record) product (Verhoef et al., 2017) are considered. The ESA CCI SST analysis is given on a regular 0.05° grid and the METOP-A ASCAT wind on its irregular along-track grid at 12.5 km nominal resolution.

Considering all the wind swaths within the spring season (from the 1st of March to the 31st of May 2010) over the Mediterranean Sea, the seasonal percentile scatter plots for the standard metrics (SST Laplacian and wind divergence) and the across-wind variables can be computed (Figure 9). It appears that a different response is detected according to the variables considered. In particular, no relationship between the wind divergence and the SST Laplacian is detected, in agreement with previous studies such as Meroni et al. (2020) and Desbiolles et al. (2021). However, a significant Spearman r correlation is found between the across-wind variables, suggesting that PA is actually at play, as found from the numerical simulations presented in this work. Thus, concluding

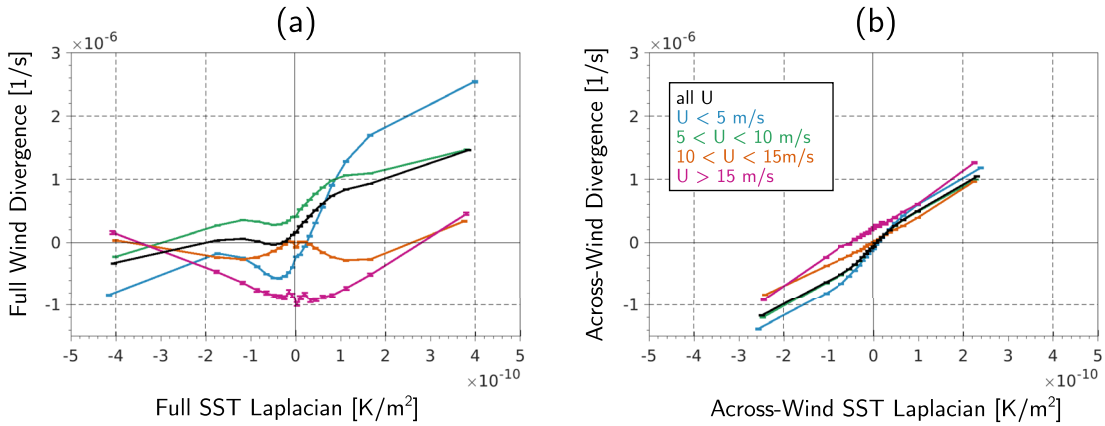

Figure 10. Percentile scatter plots (mean and standard error for each bin, shown in terms of dimensional sea surface temperature (SST) forcing) of (a) wind divergence and SST Laplacian, and (b) across-wind divergence and across-wind SST Laplacian. Global daily ERA5 data from 2007 are used and different curves correspond to different background wind speed, as indicated in the legend.

that the PA mechanism does not control the atmospheric wind response over the Mediterranean Sea might be incorrect just because the signal is masked by advection, as discussed in the previous sections. A full characterization of the wind response using these data goes beyond the scope of the present work and will be considered in a future work. Here, we can state that the newly defined across-wind metric is able to detect a PA-mediated signal even in high resolution remote sensing observational products.

Finally, we can verify a posteriori that the improved detection skills of the across-wind metrics with respect to the standard one emerge in all wind conditions and irrespective of the region considered. This is accomplished by analyzing 1 year (2007) of global daily ERA5 reanalysis data (Hersbach et al., 2020). In particular, the standard and the across-wind metrics are computed for different classes of background wind (between 0 and 5 m s^{-1}, between 5 and 10 m s^{-1}, between 10 and 15 m s^{-1}, and above 15 m s^{-1}). It appears that the signal in the across-wind metrics emerges for all background wind conditions over the globe (Figure 10), which enables to generalize the results of the present simulations, that are limited to relatively weak wind conditions and over a small region.

6. Conclusions

The PA mechanism is mostly known in the literature to produce a wind divergence response over large SST structures and relatively long scales, namely seasonal and annual (Minobe et al., 2008; Takatama et al., 2015). Evidence of its control on the wind divergence over fine-scale SST structures and short time scales has been detected either in very low or absent background wind environments (Lambaerts et al., 2013), or exploiting correlation coefficients between wind divergence and air temperature (Foussard et al., 2019), which is not easy to observe from satellites. Advection has been proposed to be the main responsible for the breaking of the correlation between SST Laplacian and wind divergence (Foussard et al., 2019), which is one of the standard PA metrics (Minobe et al., 2008; Small et al., 2008).

In this work, we introduce and test three new metrics to detect the fast action of PA exploiting SST and wind field data, only. The skills of the new metrics are evaluated using a set of high-resolution realistic numerical atmospheric simulations with appropriately modified SST forcing fields. In particular, the presence of a simulation with a uniform SST field enables to directly look at the effects of the SST spatial structures on the MABL dynamics. Among the proposed metrics, only the one based on the correlation between the across-wind SST Laplacian and the across-wind divergence, so that the masking effect of the large-scale wind advection is reduced, is able to detect the PA-mediated atmospheric response. This approach exploits the fact that pressure is a scalar and it can produce gradients in all directions. A significant Spearman r correlation between the across-wind SST Laplacian and the across-wind divergence is found when the SST forcing field has small-scale spatial structures, whereas no correlation is detected when the forcing SST field is smoothed. This is in line with the physical interpretation of the characteristic length scale of the PA-mediated response, $L_p \sim U_0 h^2/K_T$, which is large in the along-wind

direction, L_p ~100 km in the present setup, and tends to zero in the direction perpendicular to the background wind, where U_0 tends to zero. This explains why the new metrics is able to detect the PA-mediated response over short spatial scales. If the focus is on larger spatial scales, of the order of the PA adjustment scale L_p ~100 km, also smoothing the SST Laplacian and the wind divergence fields can recover the correlation. This extends the findings of Lambaerts et al. (2013) to higher background wind conditions and confirms the results of Foussard et al. (2019). Global daily ERA5 reanalysis data also show a posteriori that the across-wind metrics has improved skills in detecting the PA-mediated response with respect to the standard metric, irrespective of the background wind conditions.

An example of application of these new metrics to high-resolution satellite data in the Mediterranean Sea shows that by looking at the across-wind direction, a PA-mediated wind response emerges on sub-daily time scales, which has never been observed before using the standard metrics (Desbiolles et al., 2021; Meroni et al., 2020). Future efforts devoted to characterize the spatio-temporal variability of the PA-mediated response using satellite data at high resolution from current and future missions (such as those proposed in the European Space Agency, ESA, Earth Explorer X Harmony, ESA (2020)) will allow to better characterize air-sea feedbacks and to properly parameterize them in climate models.

Data Availability Statement

The WRF model outputs of interest can be downloaded from https://doi.org/10.5281/zenodo.5534305 (Meroni, 2021a). The L4 ESA CCI SST analysis product v2.1 is available from the Centre for Environmental Data Analysis (CEDA) archive (Good et al., 2019). The L2 coastal ASCAT METOP-A CDR wind field product (Verhoef et al., 2017) is available from the NASA JPL PODAAC platform (EUMETSAT/OSI SAF, 2018). ERA5 data have been downloaded from the Copernicus Climate Data Store (Hersbach et al., 2018). The analyses of the WRF model outputs have been carried out with a Jupyter Notebook available at https://github.com/agonmer/meroni_etal_JGRA_2022.git (Meroni, 2021b).

Acknowledgments
The authors acknowledge support from the project JPI Climate Oceans EUREC4A-OA, Progetto Dipartimenti di Eccellenza, funded by MIUR 2018-2022 and the European Space Agency (ESA) contracts 4000135827/21/NL/FF/an and 4000134959/21/NL/FF/an. A. N. M. is supported by ESA as part of the Climate Change Initiative (CCI) fellowship (ESA ESRIN/Contract No. 4000133281/20/I/NB). F. D. is supported by ESA contract n. 4000127657/19/NL/FF/gp and by HPC-TRES Grant No. 2020-10. The authors thank David E. Atkinson and an anonymous reviewer for the fruitful comments during the revision. Open Access Funding provided by Universita degli Studi di Milano-Bicocca within the CRUI-CARE Agreement.

References

Chelton, D. B., Esbensen, S. K., Schlax, M. G., Thum, N., Freilich, M. H., Wentz, F. J., et al. (2001). Observations of coupling between surface wind stress and sea surface temperature in the eastern tropical Pacific. *Journal of Climate*, *14*(7), 1479–1498. https://doi.org/10.1175/1520-0442(2001)014<1479:oocbsw>2.0.co;2

Chelton, D. B., Schlax, M. G., Freilich, M. H., & Milliff, R. F. (2004). Satellite measurements reveal persistent small-scale features in ocean winds. *Science*, *303*(5660), 978–983. https://doi.org/10.1126/science.1091901

Chelton, D. B., & Xie, S.-P. (2010). Coupled ocean-atmosphere interaction at oceanic mesoscale. *Oceanography*, *23*(4), 52–69. https://doi.org/10.5670/oceanog.2010.05

Debreu, L., Marchesiello, P., Penven, P., & Cambon, G. (2012). Two-way nesting in split-explicit ocean models: Algorithms, implementation and validation. *Ocean Modelling*, *49*, 1–21. https://doi.org/10.1016/j.ocemod.2012.03.003

Desbiolles, F., Alberti, M., Hamouda, M. E., Meroni, A. N., & Pasquero, C. (2021). Links between sea surface temperature structures, clouds and rainfall: Study case of the Mediterranean Sea. *Geophysical Research Letters*, *48*(10). https://doi.org/10.1029/2020GL091839

ESA. (2020). *Report for assessment: Earth explorer 10 candidate mission Harmony*. European Space Agency. Retrieved from https://esamultimedia.esa.int/docs/EarthObservation/EE10_Harmony_Report-for-Assessment-v1.0_13Nov2020.pdf

EUMETSAT/OSI SAF. (2018). MetOp-A ASCAT level 2 12.5-km ocean surface wind vector climate data record optimized for coastal ocean. Version 1.0 [dataset]. PO.DAAC. Retrieved from https://podaac.jpl.nasa.gov/dataset/ASCATA_L2_COASTAL_CDR

Foussard, A., Lapeyre, G., & Plougonven, R. (2019). Response of surface wind divergence to mesoscale SST anomalies under different wind conditions. *Journal of the Atmospheric Sciences*, *76*(7), 2065–2082. https://doi.org/10.1175/jas-d-18-0204.1

Frenger, I., Gruber, N., Knutti, R., & Münnich, M. (2013). Imprint of southern ocean eddies on winds, clouds and rainfall. *Nature Geoscience*, *6*(8), 608–612. https://doi.org/10.1038/ngeo1863

Gaube, P., Chickadel, C. C., Branch, R., & Jessup, A. (2019). Satellite observations of SST-induced wind speed perturbation at the oceanic submesoscale. *Geophysical Research Letters*, *46*(5), 2690–2695. https://doi.org/10.1029/2018GL080807

Good, S. A., Embury, O., Bulgin, C. E., & Mittaz, J. (2019). ESA sea surface temperature climate change initiative (SST_cci): Level 4 analysis climate data record. Version 2.1 [dataset]. Centre for Environmental Data Analysis. https://doi.org/10.5285/62c0f97b1eac4e0197a674870afe1ee6

Hayes, S., McPhaden, M., & Wallace, J. (1989). The influence of sea-surface temperature on surface wind in the eastern equatorial Pacific: Weekly to monthly variability. *Journal of Climate*, *2*(12), 1500–1506. https://doi.org/10.1175/1520-0442(1989)002<1500:tiosst>2.0.co;2

Hersbach, H., Bell, B., Berrisford, P., Biavati, G., Horányi, A., Muñoz Sabater, J., et al. (2018). ERA5 hourly data on single levels from 1979 to present [dataset]. Copernicus Climate Change Service (C3S) Climate Data Store (CDS). https://doi.org/10.24381/cds.adbb2d47

Hersbach, H., Bell, B., Berrisford, P., Hirahara, S., Horányi, A., Muñoz-Sabater, J., et al. (2020). The ERA5 global reanalysis. *Quarterly Journal of the Royal Meteorological Society*, *146*(730), 1999–2049. https://doi.org/10.1002/qj.3803

Kilpatrick, T., Schneider, N., & Qiu, B. (2014). Boundary layer convergence induced by strong winds across a midlatitude SST front. *Journal of Climate*, *27*(4), 1698–1718. https://doi.org/10.1175/JCLI-D-13-00101.1

Lambaerts, J., Lapeyre, G., Plougonven, R., & Klein, P. (2013). Atmospheric response to sea surface temperature mesoscale structures. *Journal of Geophysical Research: Atmospheres*, *118*(17), 9611–9621. https://doi.org/10.1002/jgrd.50769

Li, Y., & Carbone, R. (2012). Excitation of rainfall over the tropical western pacific. *Journal of the Atmospheric Sciences*, *69*(10), 2983–2994. https://doi.org/10.1175/jas-d-11-0245.1

Lindzen, R. S., & Nigam, S. (1987). On the role of sea surface temperature gradients in forcing low-level winds and convergence in the tropics. *Journal of the Atmospheric Sciences*, *44*(17), 2418–2436. https://doi.org/10.1175/1520-0469(1987)044<2418:otross>2.0.co;2

Ma, Z., Fei, J., Lin, Y., & Huang, X. (2020). Modulation of clouds and rainfall by tropical cyclone's cold wakes. *Geophysical Research Letters*, *47*(17). https://doi.org/10.1029/2020GL088873

Merchant, C. J., Embury, O., Bulgin, C. E., Block, T., Corlett, G. K., Fiedler, E., et al. (2019). Satellite-based time-series of sea-surface temperature since 1981 for climate applications. *Scientific Data*, *6*(1), 223. https://doi.org/10.1038/s41597-019-0236-x

Meroni, A. N. (2021a). Introducing new metrics for the atmospheric pressure adjustment to thermal structures in the ocean - Instantaneous numerical outputs [dataset]. Zenodo. https://doi.org/10.5281/zenodo.5534306

Meroni, A. N. (2021b). Introducing new metrics for the atmospheric pressure adjustment to thermal structures in the ocean–Notebook [software]. Github. Retrieved from https://github.com/agonmer/meroni_et al._JGRA_2022.git

Meroni, A. N., Giurato, M., Ragone, F., & Pasquero, C. (2020). Observational evidence of the preferential occurrence of wind convergence over sea surface temperature fronts in the Mediterranean. *Quarterly Journal of the Royal Meteorological Society*, *146*(728), 1443–1458. https://doi.org/10.1002/qj.3745

Meroni, A. N., Parodi, A., & Pasquero, C. (2018). Role of SST patterns on surface wind modulation of a heavy midlatitude precipitation event. *Journal of Geophysical Research: Atmospheres*, *123*(17), 9081–9096. https://doi.org/10.1029/2018jd028276

Meroni, A. N., Renault, L., Parodi, A., & Pasquero, C. (2018). Role of the oceanic vertical thermal structure in the modulation of heavy precipitations over the Ligurian sea. *Pure and Applied Geophysics*, *175*(11), 4111–4130. https://doi.org/10.1007/s00024-018-2002-y

Minobe, S., Kuwano-Yoshida, A., Komori, N., Xie, S.-P., & Small, R. J. (2008). Influence of the gulf stream on the troposphere. *Nature*, *452*(7184), 206–209. https://doi.org/10.1038/nature06690

Pasquero, C., Desbiolles, F., & Meroni, A. N. (2021). Air-sea interactions in the cold wakes of tropical cyclones. *Geophysical Research Letters*, *48*(2). https://doi.org/10.1029/2020GL091185

Penven, P., Debreu, L., Marchesiello, P., & McWilliams, J. C. (2006). Evaluation and application of the ROMS 1-way embedding procedure to the central California upwelling system. *Ocean Modelling*, *12*(1–2), 157–187. https://doi.org/10.1016/j.ocemod.2005.05.002

Press, W. H., Teukolsky, S. A., Flannery, B. P., & Vetterling, W. T. (1992). *Numerical recipes in C* (2nd edn). Cambridge University Press.

Redelsperger, J.-L., Bouin, M.-N., Pianezze, J., Garnier, V., & Marié, L. (2019). Impact of a sharp, small-scale SST front on the marine atmospheric boundary layer on the Iroise Sea: Analysis from a hectometric simulation. *Quarterly Journal of the Royal Meteorological Society*, *145*(725), 3692–3714. https://doi.org/10.1002/qj.3650

Renault, L., Masson, S., Oerder, V., Jullien, S., & Colas, F. (2019). Disentangling the mesoscale ocean-atmosphere interactions. *Journal of Geophysical Research: Oceans*, *124*(3), 2164–2178. https://doi.org/10.1029/2018JC014628

Schneider, N. (2020). Scale and Rossby number dependence of observed wind responses to ocean-mesoscale sea surface temperatures. *Journal of the Atmospheric Sciences*, *77*(9), 3171–3192. https://doi.org/10.1175/JAS-D-20-0154.1

Skamarock, W. C., Klemp, J. B., Dudhia, J., Gill, D. O., Barker, D. M., Huang, X.-Y., et al. (2008). *A description of the advanced research WRF version 3*. NCAR Technical Note NCAR/TN-475+STR. 113 https://doi.org/10.5065/D68S4MVH

Skyllingstad, E. D., de Szoeke, S. P., & O'Neill, L. W. (2019). Modeling the transient response of tropical convection to mesoscale SST variations. *Journal of the Atmospheric Sciences*, *76*(5), 1227–1244. https://doi.org/10.1175/JAS-D-18-0079.1

Skyllingstad, E. D., Vickers, D., Mahrt, L., & Samelson, R. (2007). Effects of mesoscale sea-surface temperature fronts on the marine atmospheric boundary layer. *Boundary-Layer Meteorology*, *123*(2), 219–237. https://doi.org/10.1007/s10546-006-9127-8

Small, R., DeSzoeke, S., Xie, S., O'Neill, L., Seo, H., Song, Q., et al. (2008). Air-sea interaction over ocean fronts and eddies. *Dynamics of Atmospheres and Oceans*, *45*(3), 274–319. https://doi.org/10.1016/j.dynatmoce.2008.01.001

Spall, M. A. (2007). Midlatitude wind stress–sea surface temperature coupling in the vicinity of oceanic fronts. *Journal of Climate*, *20*(15), 3785–3801. https://doi.org/10.1175/jcli4234.1

Takatama, K., Minobe, S., Inatsu, M., & Small, R. J. (2015). Diagnostics for near-surface wind response to the Gulf Stream in a regional atmospheric model. *Journal of Climate*, *28*(1), 238–255. https://doi.org/10.1175/JCLI-D-13-00668.1

Takatama, K., & Schneider, N. (2017). The role of back pressure in the atmospheric response to surface stress induced by the Kuroshio. *Journal of the Atmospheric Sciences*, *74*(2), 597–615. https://doi.org/10.1175/JAS-D-16-0149.1

Verhoef, A., Vogelzang, J., Verspeek, J., & Stoffelen, A. (2017). Long-term scatterometer wind climate data records. *IEEE Journal of Selected Topics in Applied Earth Observations and Remote Sensing*, *10*(5), 2186–2194. https://doi.org/10.1109/JSTARS.2016.2615873

Wallace, J. M., Mitchell, T., & Deser, C. (1989). The influence of sea-surface temperature on surface wind in the eastern equatorial Pacific: Seasonal and interannual variability. *Journal of Climate*, *2*(12), 1492–1499. https://doi.org/10.1175/1520-0442(1989)002<1492:tiosst>2.0.co;2

Wenegrat, J. O., & Arthur, R. S. (2018). Response of the atmospheric boundary layer to submesoscale sea surface temperature fronts. *Geophysical Research Letters*, *45*(24), 13505–13512. https://doi.org/10.1029/2018GL081034